JOURNAL OF PROPULSION AND POWER
Vol. 21, No. 6, November–December 2005

Transient Grating Spectroscopy in a Hot Turbulent Compressible Free Jet

S. Schlamp* and T. Rösgen†
Swiss Federal Institute of Technology, 8092 Zurich, Switzerland
D. N. Kozlov‡
A.M. Prokhorov General Physics Institute, 119991, Moscow, Russia
and
C. Rakut,§ P. Kasal,¶ and J. von Wolfersdorf**
Stuttgart University, 70569 Stuttgart, Germany

Speed of sound profiles of an unseeded hot, supersonic, axisymmetric free air jet at atmospheric pressure are measured with 2% uncertainty using laser-induced electrostrictive gratings. Signal level and lifetime decay with increasing temperature, and no data are obtained for static temperatures above 540 K. The influence of temperature, turbulence, beam steering, and mechanical vibrations on the signal amplitude and lifetime is examined quantitatively. It is argued that electrostrictive gratings are applicable for thermometry and velocimetry in supersonic combustors by employing a powerful pulsed infrared probe beam. The significantly larger beam power raises the signal level by three orders of magnitude, whereas the longer wavelength reduces the effects of beam steering by increasing the angular separation between probe and signal beam.

Nomenclature

a	=	speed of sound
C_p	=	specific heat capacity at constant pressure
D	=	nozzle diameter
D_T	=	thermal diffusivity
Fr	=	Froude number
f_B	=	Brillouin frequency
g	=	constant of gravity
k	=	thermal conductivity
L	=	signal amplitude
M	=	Mach number; number of oscillations in signal
$\mathcal{M}$	=	molar mass, 28.85 g/mol for air
$\max_i$	=	intensity at ith (local) maximum in signal
$\min_i$	=	intensity at ith (local) minimum in signal
N	=	number of single-shot signals in a shot-averaged signal
p	=	pressure
$\mathcal{R}$	=	universal gas constant, 8.3145 J/(mol · K)
Re_D	=	Reynolds number based on nozzle diameter
r	=	radial coordinate
T	=	temperature
t	=	time
x, y, z	=	Cartesian coordinates
Γ	=	acoustic damping coefficient
γ	=	ratio of specific heats
θ	=	excitation laser crossing angle
Λ	=	interference fringe spacing
λ_{exc}	=	excitation laser wavelength
λ_{int}	=	interrogation laser wavelength
μ	=	dynamic viscosity
ν	=	kinematic viscosity
ρ	=	density
σ_L	=	shot-by-shot signal amplitude fluctuations due to beam steering
σ_T	=	turbulent temperature fluctuations
τ_B	=	inverse Brillouin frequency
τ_Γ	=	characteristic decay time of acoustic damping
τ_Ω	=	characteristic decay time associated with finite beam size effects
ψ	=	Bragg angle
Ω	=	characteristic beam waist diameter
$\langle\,\rangle$	=	statistical mean

Subscripts

av	=	averaged
exit	=	conditions at nozzle exit
fit	=	result from fitting routine
signal	=	exctraced from signal
weighted	=	intensity weighted by temperature

Received 4 October 2004; revision received 31 December 2004; accepted for publication 3 January 2005.

*Postdoctoral Candidate, Institute of Fluid Dynamics, Department of Mechanical and Process Engineering, ETH Zürich, Sonneggstrasse 3; schlamp@ifd.mavt.ethz.ch. Member AIAA.

†Professor, Institute of Fluid Dynamics, Department of Mechanical Engineering, ETH Zürich, Sonneggstrasse 3.

‡Senior Research Scientist, Russian Academy of Sciences, Optical Spectroscopy Department, 38 Vavilov Street.

§Graduate Student, Institute of Aerospace Thermodynamics, Department of Aerospace Engineering, Pfaffenwaldring 31.

¶Senior Research Scientist, Institute of Aerospace Thermodynamics, Department of Aerospace Engineering, Pfaffenwaldring 31.

**Professor, Institute of Aerospace Thermodynamics, Department of Aerospace Engineering, Pfaffenwaldring 31.

I. Introduction

LASER-INDUCED grating (LIG) thermometry/velocimetry is a nonintrusive, nonlinear flow diagnostic point measurement technique that can be used for the instantaneous measurement of the speed of sound and one velocity component simultaneously. No seeding with particles or tracer molecules is required. In the literature, it is also referred to as laser-induced thermal acoustics or transient grating spectroscopy.

The technique has been applied for accurate speed of sound and thermodynamic transport measurements in fluids at rest,[1–6] in high-pressure flames with soot,[7,8] as well as for velocimetry in sub- and supersonic flows.[9–17]

The signal-to-noise ratio (SNR) increases with increasing pressure and decreases with increasing temperature. Turbulence and

convective effects also degrade the SNR. The cited measurements in flames were conducted at elevated pressures, that is, temperature and pressure effects (partially) offset each other. The cited measurements in compressible and/or turbulent flows were conducted at atmospheric temperatures or below.

Flow diagnostic techniques for supersonic combustors must instead be capable to measure in highly turbulent, compressible flows at >2000 K and (sub-) atmospheric pressures. Measurements in a hot, compressible turbulent freejet are used to quantify the influence of turbulence, beam steering, convective effects, and environmental conditions on the SNR (Secs. III and IV). Section V contains a discussion of systematic errors once data have been obtained.

The work covered in this paper was initially intended to apply LIG thermometry to a heated, chemically reacting, supersonic freejet. It soon became clear that these objectives were unattainable with the available equipment and the approaches described in the literature. Based on the data acquired and observations made during this measurement campaign, challenges and opportunities for the application of LIGs to supersonic combustors are addressed in Secs. VI and VII, respectively. The observations made and the analysis of the reasons behind this initial failure provide useful guidelines for future attempts.

Several authors have successfully applied coherent anti-Stokes Raman scattering (CARS) to a scram-jet flow to measure species concentrations and temperatures. (See, for example, Ref. 18 and references therein.) CARS shares some challenges with the LIG technique, for example, that three laser beams going through a turbulent compressible flow have to be focused on the same point in space. The measurement time, however, is only the duration of the laser pulse (~10 ns) instead of $\mathcal{O}$(100 ns). Convective and turbulent effects are negligible over this timescale. The advantage of the LIG technique, if it can be made applicable to the same flows, lies in its reduced hardware requirements (no dye lasers) and that it can potentially measure the flow Mach number directly. Other nonintrusive techniques that have been performed in supersonic combustion are laser-induced fluorescence, for example, by McIntyre et al.,[19] and filtered Rayleigh scattering, for example, by Forkey et al.[20] These last two techniques are for imaging, that is, they provide data for an entire plane, which requires sufficient optical access, but they suffer from sensitivity to flow luminosity.

II. Laser-Induced Transient Gratings

Two pulsed, intersecting focused laser beams produce an interference fringe pattern in the sample volume. The pulse energies are sufficient to produce a nonresonant fluid response in the form of spatially periodic density perturbations by means of electrostriction. The fringe spacing is related to the excitation laser wavelength and the laser beam crossing angle by

$$\Lambda = \lambda_{\text{exc}}/2\sin(\theta/2) \tag{1}$$

The density perturbations propagate in opposite directions as two acoustic wave packets, which initially cancel out. Subsequently, they interfere constructively and destructively with each other. The characteristic frequency is called the Brillouin frequency,

$$f_B = a/\Lambda \tag{2}$$

As the density perturbations leave the sample volume, they decay by dissipative processes (heat conduction and viscosity). The acoustic damping coefficient is a measure for the dissipative effects. For a quiescent perfect gas, it is[21]

$$\Gamma = (1/2\rho)\left[(\gamma-1)(k/C_p) + \tfrac{4}{3}\mu\right] \tag{3}$$

which can be rewritten as

$$\Gamma = \tfrac{1}{2}\left[(\gamma-1)D_T + \tfrac{4}{3}\nu\right] \tag{4}$$

Spatially periodic density perturbations can also be achieved as a result of resonant absorption in the fluid by either resonantly pumping the test fluid (in the ultraviolet for nitrogen and oxygen) or by seeding the flow, for example, with nitric oxide or iodine vapor. Thermalization, which follows the absorption, in addition to generation of the acoustic waves, leads to an additional, stationary (with respect to the fluid) density perturbation. It interferes with the acoustic waves, and it decays by means of thermal diffusion. In both cases, that is, at nonresonant or resonant excitation, all density perturbations result in temporally and spatially varying modulations of the refractive index, called electrostrictive and thermal LIG, respectively. A small fraction of a second, continuous-wave laser beam (interrogation beam, $\lambda_{\text{int}} \neq \lambda_{\text{exc}}$), directed at the grating's Bragg angle

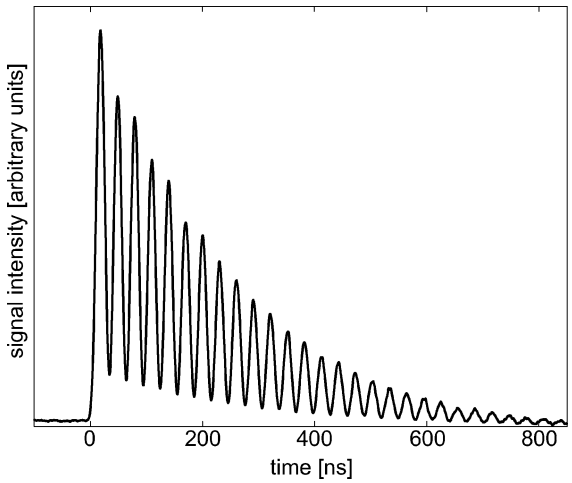

Fig. 1 Intensity of signal beam vs time (typical data for electrostrictive gratings and ambient air, averaged over 512 excitation laser pulses).

$$\psi = (\lambda_{\text{int}}/\lambda_{\text{exc}})\theta \tag{5}$$

on the sample volume is coherently diffracted into a signal beam. The intensity of the signal beam depends on the instantaneous amplitude of the density perturbations. The Doppler shift of the signal beam frequency can be detected by heterodyning, that is, by superimposing a fixed-frequency reference beam onto the signal beam and measuring the frequency difference as beat note. The speed of sound and flow velocity can then be extracted from the time history of the recorded signal. The speed of sound and the flow velocity are encoded as the Brillouin frequency (Fig. 1) and the Doppler frequency shift, respectively. Mixtures and harmonics of these frequencies can be present in the signal's power spectrum.[9,14] Note that in Fig. 1 the frequency of the oscillations is twice the Brillouin frequency. The decay is governed by the finite beam sizes and by dissipative processes. This signal was recorded before facility startup.

III. Experimental Setup and Procedure

A. Flow Facility

This paper is the result of experiments conducted in the supersonic combustor facility at Stuttgart University, Germany. It is described in more detail in Refs. 22 and 23. A two-stage, 600-kW compressor (1.45 kg/s, $p_{\max} = 10.5$ bar) supplies air with $p = 3.35$ bar (absolute) to the electrical heating elements (1 MW, $T_{\max} = 1500$ K), which heat the air to a stagnation temperature of $T_0 = 1365$ K. The air is accelerated to $M = 1.45$ in a converging–diverging nozzle (Fig. 2). Hot air flows through the space between the inner and outer nozzles. Hydrogen or cooling air is injected through the central nozzle. Note that the flow velocities are not matched. The Reynolds number based on the nozzle diameter and the fluid properties at the nozzle exit is

$$Re_D = \frac{u_{\text{exit}} D}{\nu(T_{\text{exit}})} = 2.5 \times 10^5 \tag{6}$$

The Froude number relates the inertial to buoyancy forces. For the exit conditions of the hot jet it is[24]

$$Fr = \frac{\rho_{\text{exit}} u_{\text{exit}}^2}{g D(\rho_{\text{amb}} - \rho_{\text{exit}})} = 1.3 \times 10^6 \tag{7}$$

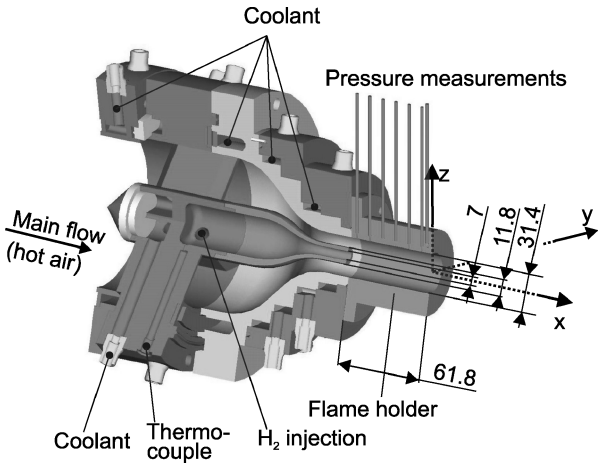

Fig. 2 Cut-away of supersonic nozzle (all dimensions in millimeters).

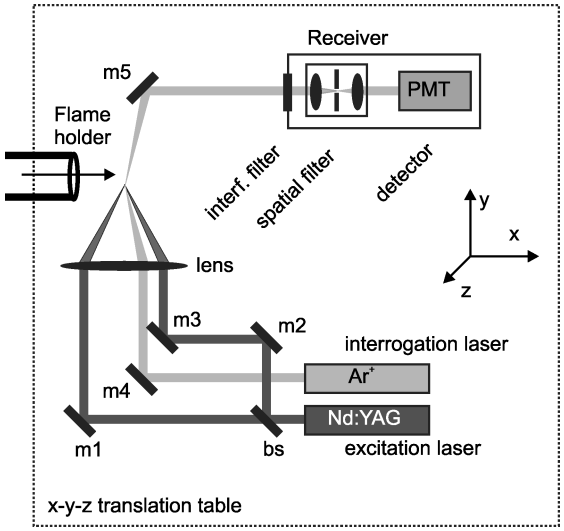

Fig. 3 Schematic of the optical setup: beam splitter, bs; mirror, *m*; and photomultiplier tube (PMT).

Buoyancy can, thus, be neglected, that is, the jet is axisymmetric. Cooling air or hydrogen are supplied through a central nozzle with choked exit conditions (7-mm inside and 11.8-mm outside diameter). A flame holder (length of 61.8 mm and $D = 31.4$ mm) is smoothly attached to the exit plane of the two concentric nozzles. A shock and expansion wave structure forms between the exit of the nozzles and the exit of the flame holder. The exit pressures of the coolant flow and the supersonic main flow are atmospheric. Therefore, these waves are weak.

Experiments were performed under four different run conditions: 1) off, compressor off, no flow, and no vibrations; 2) no flow, compressor running, flow going through bypass line; 3) hot jet, coolant air through central nozzle; and 4) flame, H_2 injection through central nozzle (combustion).

B. Optical Setup

Figure 3 shows the experimental setup schematically. A frequency-doubled, Q-switched Nd:YAG (JK Lasers, System 2000, $\sim$100 mJ at 532 nm, 10 ns, and 10 Hz) serves as the excitation laser. A 50/50 beam splitter (bs) and mirrors m1, m2, and m3 direct the two beams path-length matched and parallel to each other onto the lens with focal length $\ell = 1000$ mm. Mirror m4 directs the continuous-wave interrogation beam from an argon-ion laser (Spectra-Physics BeamLok 2080, 488 nm and 6 W) onto the same lens so that it intersects the interference fringes at the Bragg angle. Mirror m5 intercepts the signal beam and directs it into the receiver unit, where it passes a 488-nm interference filter (0.2-nm linewidth) and a spatial filter (50-μm pinhole diameter) before reaching the detector (Hamamatsu H6780, 0.78-ns rise time).

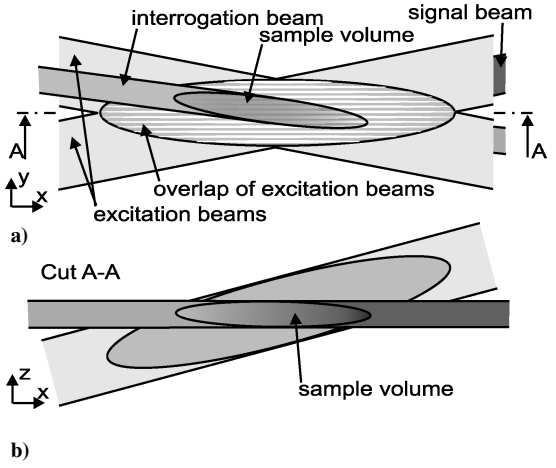

Fig. 4 Sample volume (not to scale): a) top and b) side view.

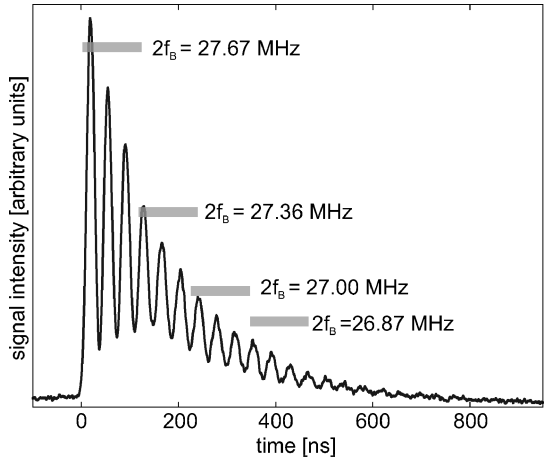

Fig. 5 Brillouin frequency appears to decrease over lifetime of this electrostrictive signal; Gaussian beam waist radius of excitation and interrogation beams are 270 and 100 μm, respectively.

The sample volume is defined by the region where the two excitation beams and the interrogation beam overlap (Fig. 4). The overlap volume of the excitation beams is an elongated ellipsoid, because of the Gaussian beam profiles. The intersection between this ellipsoid and the interrogation beam is the sample volume. The focusing diameters of the excitation and interrogation beams varied. For the signal shown in Fig. 5, the excitation beam waist diameter is estimated to be 540 μm and that of the interrogation beam to be 200 μm. These values are typical for other data series. The smaller value corresponds to the characteristic height and width of the sample volume. An excitation beam crossing half-angle of $\theta/2 = 0.75$ deg was used. This results in an interference fringe spacing of $\Lambda = 20$ μm. The interrogation beam intercepts the ellipsoidal intersection region of the excitation beams at an angle. (See discussion in Sec. VI.B.) For the case shown in Fig. 5, this angle is approximately 1.5 deg. This reduces the length of the sample volume to approximately 10 mm. All data presented in Sec. IV were obtained with this set of parameters.

The entire optical setup is located on a three-axes translation table. The origin of the coordinate system is chosen to be the center of the flame holder exit. The x axis is aligned with the flow, and the y and z axes are in the horizontal and vertical direction, respectively. A high-speed photodiode (Thorlabs DET 210, 1-ns rise time, not shown in Fig. 3) detects the excitation laser pulse and triggers the data acquisition. The output of the photomultiplier tube is amplified by a high-bandwidth current-to-voltage converter (Hamamatsu C5594, bandwidth 50 kHz–1.5 GHz) and recorded by a digital storage oscilloscope (LeCroy WaveRunner LT374L, 500-MHz bandwidth). The

power supplies for the detector and the amplifier were contained in the metallic receiver unit. Signal cables were double shielded.

The stability of the optical setup with respect to vibrations was achieved only after several iterations until the signal amplitude remained constant over several hours as long as no hydrogen was injected. Because of vibrations, a recalibration was necessary after a few 30-s H_2 injection (combustion) cycles.

C. Procedure

The optics were aligned before the facility's main valve separating the 600-kW compressor from the nozzle, was opened (no flow, Sec. III.A). The compressor itself, which is located at a distance of 30 m from the nozzle, causes only minimal vibrations in the jet facility. The vibrations of the optical setup are predominantly induced by the noise of the freejet after the main valve has been opened. Vibrations are, thus, negligible during this initial alignment. The relative position of the reference frame (origin at the flame holder exit) in the coordinate system of the translation table was determined. By design, the axes of movement of the translation table are collinear and perpendicular to the jet direction.

The freejet was then started, and the temperature of the heating elements was raised over a period of 2 h to achieve the desired reservoir conditions of $T_0 = 1365$ K and $p_0 = 3.35$ bar (absolute). The optics were then realigned to maximize the detected signal amplitude. The location of the sample volume shifts in the y direction when the inside of the hot jet is probed (Sec. V.B) because of the change in index of refraction of the hot vs the cold air. To compensate for this effect, the translation table was moved in the y direction until the distance between the excitation beams measured in front of and behind the jet ($y/D = \pm 2$, $x/D \approx 0$) was the same. Refraction within the hot jet typically shifted the sample volume by 5 mm in the y direction. The other spatial directions were not affected.

Radial profiles at different downstream locations x were measured starting outside the jet, moving toward the centerline. The distance between measurement locations was 10 mm for $r = 100, \ldots, 60$ mm, 5 mm for $r = 55, \ldots, 30$ mm, and 2.5 mm for $r \leq 27.5$ mm. The data were averaged over 512 excitation laser shots. Before each profile, a signal was recorded at a quiescent location outside the region of influence of the jet. This signal was used for the calibration of the fitting technique. (See Sec. III.D.)

D. Data Analysis

After removal of the baseline shift introduced by the amplifier, the signals were processed by a fitting technique, in which a theoretical model is least-squares fitted to the experimental data. The speed of sound is one of the free parameters. Fitting solely in the frequency domain with Prony's method was used by Hart et al.[25] Fitting solely in the time domain was used for example, by Cummings et al.[26] Here, the fitting is done in two steps: First, the power spectrum of the signal is fitted to the power spectrum of the theoretical model (as given in Ref. 26). The speed of sound, the signal damping rate, and a multiplicative constant accounting for variations in the signal amplitude are the fitting parameters. The results for those are then used as initial guesses during the second step, which is applied to the signal in the time domain. For both steps, the Levenberg–Marquardt algorithm was employed. In quiescent fluids, the measured signal damping rate is equal to the acoustic damping rate because the decay due to the finite beam size effects is treated separately, that is, the signal decays approximately as

$$\exp[-\Gamma_{\text{signal}} t - (at/\Omega)]^2, \qquad t \geq 0 \tag{8}$$

where a is the local speed of sound and Ω denotes a characteristic beam waist radius that incorporates the beam waist radii of the excitation beams and the interrogation beam. (See Ref. 26 for a more detailed treatment.) A similar two-step approach had been used previously by Hart et al.[9] It was found that the fitting in the frequency domain is more robust, but that the fitting in the time domain is more accurate.

The excitation beam crossing angle and the excitation and interrogation beam waist radii are additional important parameters in the model. They are found from the calibration measurement where the speed of sound and the acoustic damping rate are known. The beam crossing angle and the Gaussian beam waist radii are used as free parameters instead of the speed of sound and the acoustic damping rate.

Hart et al.[9] observed a frequency chirp when the diameter of the interrogation beam was larger than the diameter of the excitation beam. The authors explain their observation by the changing scattering angle with respect to the detector as the density perturbations are convected across the interrogation beam's focus region. Such a chirp has also been observed in some signals in the present study (Fig. 5), where the Gaussian waist radii of the excitation and the interrogation beams are estimated to be 270 and 100 μm, respectively. This contradicts the condition just given. The error bars on the beam radii, however, are large. The mechanism responsible for the chirp in the present measurements is, thus, not clear. Slow cooling of the probe volume that is heated as a result of the adiabatic compression by electrostriction could also be considered. This could be verified by varying the excitation pulse energy. Another alternative explanation are deviations from the plane-wave assumption, that is, that the motion of the acoustic waves is not one dimensional. One rather has to consider the wave packets as a collection of (three-dimensional) acoustic point sources. This could particularly be true for small beam diameters and small beam crossing angles, that is, where the beam waist diameter is not too much larger than the fringe spacing. Also, this would lead to the observed sign of the chirp and is also consistent with the fact that it was only observed for long-lifetime signals. The intermittency of the chirp is not explained by either explanation. Shot-by-shot fluctuations of the excitation laser should not play a role because all signals are averaged over several hundred shots.

In Fig. 5, the oscillation frequency is determined within different time windows (gray stripes). The signal shown was acquired at $x/D = 15.9$ and $r/D = 3$. The chirp could only be observed for signals with longer lifetimes, that is, from slow, colder regions on the shoulders of the jet. When it was observed, the chirp did not exceed 3%, and the beating frequency always decreased over the signal lifetime. The latter point is consistent with the analysis of Hart et al.,[9] who make a connection between the chirp and the flow direction. If the frequency chirp was due to temperature fluctuations during the signal lifetime, then the chirp would be observed in both directions. Shot-to-shot temperature fluctuations do not produce a frequency chirp (Sec. V.D). Hence, the fitting routines were applied to the first three signal oscillations only.

IV. Results

Figure 6 shows signals at several radial positions at the axial location $x/D = 15.9$. The signal amplitude and the lifetime both decrease when approaching the centerline of the jet. The centerline temperature at this x/D is 480 K. Even outside the jet (trace A), the signal lifetime and SNR are less than for a signal recorded on

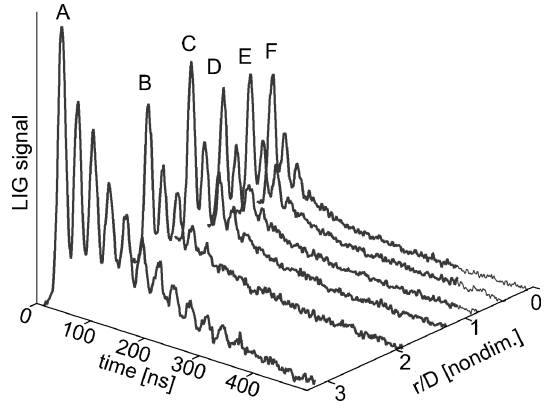

Fig. 6 LIG signals at different radial locations where labels correspond to labels in Figs. 7–9 and 11; series shows below-average drop in signal amplitude (see Fig. 11).

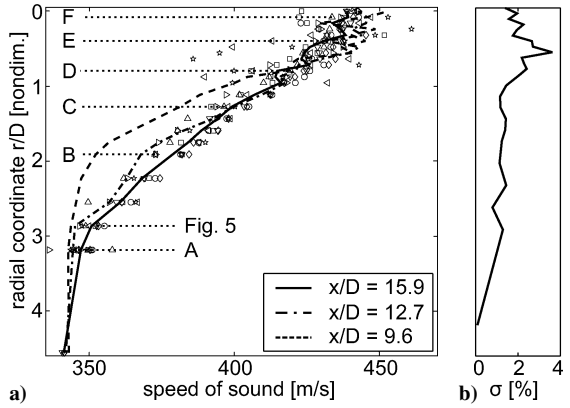

Fig. 7 Speed of sound profiles through a hot, initially supersonic, highly turbulent, axisymmetric jet of air; stagnation temperature and pressure are 1365 K and 3.35 bar absolute, respectively.

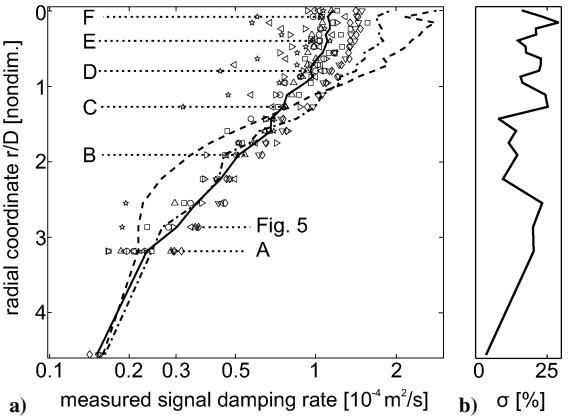

Fig. 8 Radial profiles of the signal damping rate; contributions are from viscosity, heat conduction, eddy diffusivity, and convective effects.

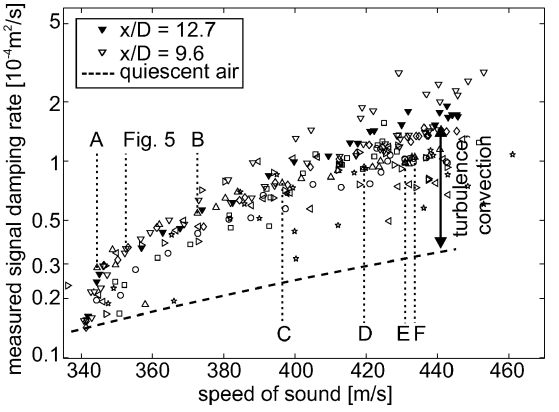

Fig. 9 Signal damping rate vs speed of sound; open symbols for *x/D* = 15.9; excess signal damping can be attributed to eddy diffusivity and convective effects.

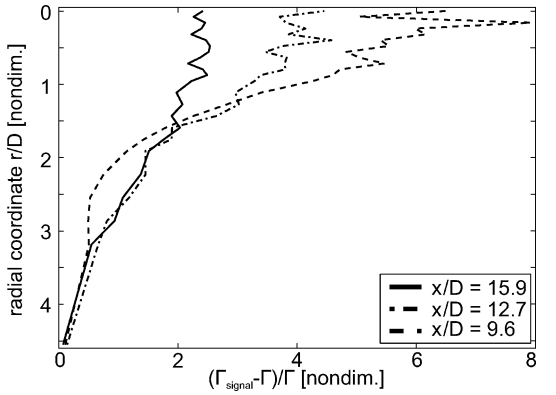

Fig. 10 Contribution of turbulence and convection to signal damping rate relative to acoustic damping rate for quiescent air.

the same day before the compressor and flow were started (Fig. 1). Note that the drop in signal amplitude in signals A–F is less than typical.

Speed of sound profiles are shown in Fig. 7 for different axial locations. Note that the temperature is proportional to the square of the speed of sound. Results from several measurement series are shown at $x/D = 15.9$. The signals, which correspond to the labeled data points, are plotted in Fig. 6. Averaging was performed over 128 laser pulses in three of the series, over 512 pulses in the remaining series. In two of the former, the averaged data were stored with only 8-bit resolution. Digitizing noise was significant in these instances. Still, including these data, the relative uncertainty for the speed of sound data is below 2% almost everywhere. The standard deviation of the speed of sound data at $x/D = 15.9$ is shown in Fig. 7b. Also shown are individual profiles acquired farther upstream at $x/D = 12.7$ and 9.6. The radial spreading and the increase of the centerline temperature is apparent.

The measured signal damping rate is shown in Fig. 8. Figure 8b shows the uncertainty, which is one order of magnitude larger than for the sound speed data. The large discrepancy between the uncertainties of the speed of sound and the acoustic damping rate data is consistent with prior work.[3,27] The effects of turbulence and convection of the grating with the mean flow are not treated separately in the data analysis. Eddy diffusivity and thermal diffusivity cannot be distinguished. Introduction of the flow velocity as an additional free fitting parameter led to unreasonable results.

The measured signal damping rate profiles are plotted vs the speed of sound in Fig. 9. The signal damping rate is a measure of the signal lifetime (for fixed-beam diameters), higher signal damping rates corresponding to shorter signal lifetimes. The dashed line represents the acoustic damping rate for quiescent air at atmospheric pressure using values of temperature recalculated from data in Fig. 7. It is interpolated from tabulated data of $D_T(T)$ (Ref. 28) and a regression for $\mu(T)$ (Ref. 29) in Eq. (4).

The calibration measurements are performed in quiescent air. The tabulated values for the thermal diffusivity and the viscosity are used to derive the beam waist diameters. When the same signal is analyzed first with fixed acoustic damping coefficient to obtain the beam diameters and then with these beam diameters, one expects to recover the original acoustic damping rate. The good agreement in Fig. 9 outside of the jet, where the conditions are similar to those of the calibration measurements, are, thus, a consequence of the calibration procedure. The accelerated decay inside the jet can be attributed to the influence of turbulence and convection. For smaller x/D, these effects become more important, that is, given two points at different x/D but with the same temperature (downstream point being, thus, closer to the jet centerline), turbulence and convection are more significant at the more upstream point.

Figure 10 combines the information from Figs. 7–9. It shows the contributions of turbulence and convection in excess to those of heat conduction and viscosity to the acoustic damping rate. Turbulence and convective effects dominate for $r/D < 2$. At $x/D = 9.6$, their contribution is eight times stronger than that of heat conduction and viscosity alone.

The maximum signal intensities (first signal peak) from all data shown in Figs. 7 and 8 are plotted vs the speed of sound in Fig. 11. The amplitudes of the traces shown in Fig. 6 are not representative. The intensities are normalized by the intensity of the calibration signal of each data series. The scatter is considerable. The solid line is a power-law fit to the data points. The intensity scales as $T^{-4.25}$. Danehy[30] predicts a p^2T^{-3} dependence for electrostrictive signals at constant pressure in quiescent fluids. The dashed line shows this dependence. Note that, to our knowledge, the T^{-3} dependence has not been verified experimentally. Hart et al.[31] do not provide results for the signal intensity vs temperature. Provided that the T^{-3}

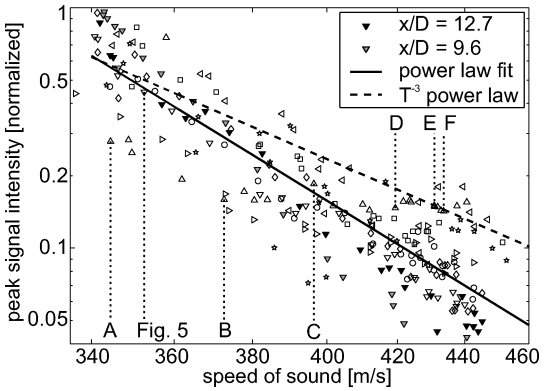

Fig. 11 Peak signal intensity vs measured speed of sound for all data points in Figs. 7 and 8; The open symbols for $x/D = 15.9$.

dependence is correct for quiescent fluids, the excess signal loss can be attributed to beam steering effects. Turbulence, convective effects, and acoustic damping act over longer timescales and only have a negligible effect on the peak intensity, which is observed for the first peak of a signal. Figure 11 shows that the intensities decay more quickly as one approaches the nozzle. The exponent depends on the correlation between temperature and the magnitude of the turbulent density perturbations. In particular, it depends on the geometry, on the Reynolds number, and on the ratio of the jet to the ambient temperature. In the present case, the level of turbulence increases toward the jet center, as does the temperature.

V. Systematic Errors

A. Misalignment

The Brillouin frequency can be extracted very accurately from the data even at moderate SNRs. Systematic errors can occur in the conversion step from Brillouin frequency to speed of sound. The most important parameter is the excitation beam crossing angle. It is obtained in a calibration measurement at a known speed of sound (Sec. III.D). When the beam crossing angle changes between the time of the calibration and the time of the measurement, or when the assumed temperature in the calibration is erroneous, a systematic error is observed. Such a change could be caused by gradual misalignments of the optics due to vibrations. Calibration measurements were, thus, made just before and just after each profile. The difference in the beam crossing angles was typically less than 0.3%. Part of the observed error could be due to actual changes of the ambient temperature between the two calibration measurements (20 min apart).

Note that refraction due to the density variation in the jet changes the beam crossing. Under the assumption that both excitation beams are affected equally, that is, neglecting streamwise density gradients, this is exactly compensated by a corresponding change of the wavelength. The interference fringe spacing in the sample volume is not affected. (See also Sec. V.B.)

B. Measurement Location

The sample volume shifts due to density gradients associated with the mean temperature profile (Fig. 12). Assume that one starts measuring at a point on the z axis, outside the jet. If the translation table is moved radially inward, then the measurement location is shifted in the direction of the laser beams (y direction). The amount of this error is not known a priori, but depends on the density profile. When the jet is axisymmetric, one could compare the spacing between the two excitation beams before and after passing the jet at known radial locations. Theoretically, an iterative approach is feasible, where corrections are based on the measured temperature profile from the preceding iteration. Practically, both approaches are difficult to implement and are time consuming.

As described in Sec. III.C, the location of the measurement volume was calibrated immediately behind the flame holder, where the jet has not yet spread radially and where errors of the measurement

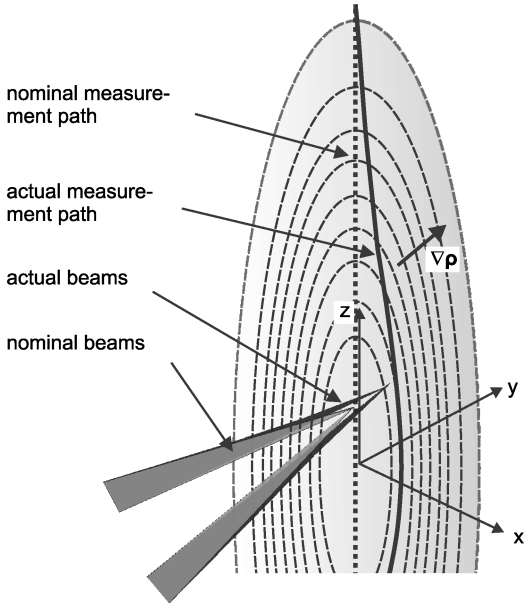

Fig. 12 Excitation beams are bent due to reduced densities inside hot jet, resulting in erroneous measurement location (error in y direction); measurement locations follow path of thick solid line instead of that of thick dashed line.

location are most significant. The measurement location shifted by $\sim$5 mm ($<0.2D$) when the hot jet was present (Sec. III.C). Farther downstream, the jet has spread radially, but the density gradients are smaller. The magnitude of the location error there is expected to be comparable in absolute terms, that is, smaller with respect to the local jet diameter.

The location error is also comparable to the length of the measurement volume. The measured speed of sound is a nonlinear average over the sample volume.

C. Beam Widths

The decay terms for the signal damping rate [$\sim\exp(-t)$] and the finite beam sizes [$\sim\exp(-t^2)$] cannot be distinguished adequately by their different temporal behavior. To determine the signal damping rate to acceptable accuracy, the beam waist diameters are estimated in the calibration procedure and assumed constant in the measurement. When the spot size within the jet differs from that in the calibration measurement, then errors of the measured signal damping rate result. It seems unlikely that the spot size within the jet is smaller than in quiescent air. If the actual beam waist diameters are larger than the assumed values, then the oscillations in the signal decay more slowly than expected. The measured signal damping rate is, thus, smaller than the actual value. The effect seen in Fig. 9 cannot be explained by increased spot sizes, which would have instead the effect of underpredicting the signal damping rate.

The sensitivity of the measured signal damping rate data to errors of the beam waist radii depends on the acoustic damping rate of the fluid. If the timescale of the acoustic damping is much larger than the signal lifetime, for example, in quiescent, low-pressure gases, then the finite beam sizes govern the signal decay. In highly dissipative environments, however, the effects of the finite beam sizes are negligible. In the case of the freejet, the higher the level of turbulence and the potential change of beam diameters, the lower the sensitivity to this error.

D. Shot Averaging

As mentioned earlier, Danehy[30] showed that, for electrostrictive signals, the signal intensity scales as p^2T^{-3}, where p is the fluid pressure and T is the temperature. This introduces a systematic error when one averages over multiple shots because shot-to-shot temperature fluctuations lead to an overrepresentation in the averaged signal of those realizations from colder, higher-pressure realizations. The speed of sound and the acoustic damping rate obtained from

analyzing the averaged signal are not the true statistical averages of these quantities.

Assume a mean temperature $\langle T\rangle$. When the theoretical model from Ref. 26 is used, $N = 1000$ electrostrictive signals are calculated (each consisting of 2000 data points over 1 μs), where the temperature varies (normal distribution) around $\langle T\rangle$. The temperature is assumed to be constant during the signal lifetime, that is, only intersignal temperature fluctuations are considered. Quiescent air and atmospheric pressure is assumed for the fluid, that is, the pressure does not fluctuate. The ideal gas relation $a = \sqrt{(\gamma \mathcal{R} T/\mathcal{M})}$ is used for the derivation of the gas temperature. The excitation (532-nm) and interrogation (488-nm) beam waist radii are assumed to be 300 μm, and the excitation beam crossing half-angle is 0.75 deg. The standard deviation of the shot-to-shot temperature fluctuations is σ_T. The nominal acoustic damping rate for each signal is found from Eq. (4). Each signal is initially normalized to a peak amplitude of unity. An averaged signal L_{av} is then calculated according to

$$L_{\text{av}} = \sum_{i=1}^{N} \left(\frac{T_i}{\langle T\rangle} \right)^{-3} L_i \tag{9}$$

where each signal L_i is weighted to mimic the overrepresentation of signals from colder realizations.

The theoretical model is fitted to the averaged signal using a Levenberg–Marquardt algorithm in the time domain. The speed of sound, the acoustic damping rate, and a multiplicative constant are the only free parameters. The other parameters are set to the correct values. The resulting speed of sound and the acoustic damping rate are compared with $a(\langle T\rangle)$ and $\Gamma(\langle T\rangle)$.

The error for the speed of sound for different relative fluctuation magnitudes and mean temperatures is plotted in Fig. 13. The error is defined as

$$\frac{\Delta a}{a} = \frac{a_{\text{fit}} - a(\langle T\rangle)}{a(\langle T\rangle)} \tag{10}$$

where a denotes the speed of sound and a_{fit} is the measured speed of sound as obtained from the fitting routine. Each line in Fig. 13 represents a different $\langle T\rangle$ from the range $\langle T\rangle = 283, \ldots, 473$ K. No temperature dependence is observed. The differences are statistical in nature and are mostly due to outliers within a dataset of $N = 1000$ signals. The bias toward lower measured sound speeds increases with the magnitude of the temperature fluctuations. For temperature fluctuations of $\sigma_T = 10\%$, the speed of sound is underpredicted by 2% and temperatures, thus, by 4%.

The dashed line in Fig. 13 indicates the deviation of the average speed of sound, for example, obtained from averaging over several single-shot signals

$$\langle a\rangle = \frac{1}{N} \sum_{i=1}^{N} \Lambda f_{B,i} \tag{11}$$

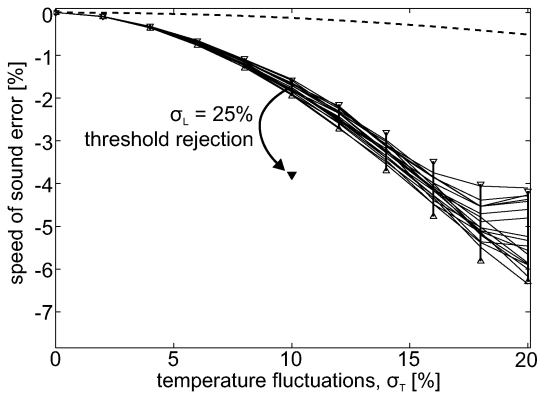

Fig. 13 Error [as given by Eq. (10)] of measured speed of sound vs standard deviation of temperature fluctuations, where each line corresponds to a different mean temperature: - - - -, deviation of average speed of sound from speed of sound at average temperature.

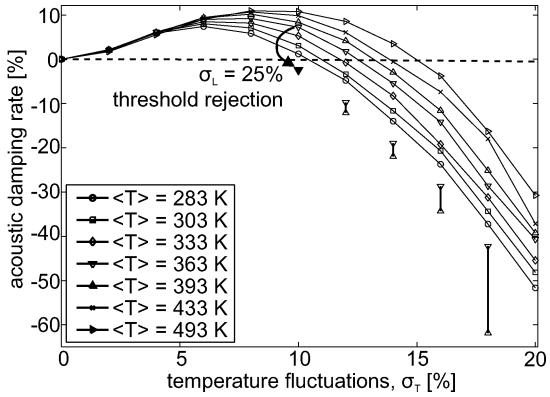

Fig. 14 Error [as given by Eq. (12)] of measured acoustic damping rate vs standard deviation of temperature fluctuations for different mean temperatures: - - - -, deviation of average acoustic damping rate from acoustic damping rate at average temperature; error bars for $\langle T\rangle$ = 363 K shifted for clarity.

from $a(\langle T\rangle)$, where f_B is the Brillouin frequency, $f_B = a/\Lambda$. Because of the nonlinear sound speed–temperature dependence, the speed of sound at the average temperature is not identical to the average speed of sound. This contribution to the measurement error is negligible compared to the effect that the temperature has on the signal intensity. A chirp of the Brillouin frequency as shown in Fig. 5 is not observed in the averaged signals.

The corresponding influence on the measured acoustic damping rate is shown in Fig. 14. Analogous to Eq. (10), the expression

$$\frac{\Delta \Gamma}{\Gamma} = \frac{\Gamma_{\text{fit}} - \Gamma(\langle T\rangle)}{\Gamma(\langle T\rangle)} \tag{12}$$

is used for the error of the acoustic damping rate. Γ is overpredicted for low values of σ_T and underpredicted for larger σ_T. The crossover value of σ_T depends on $\langle T\rangle$. For $\langle T\rangle = 303$ K, the error changes sign at $\sigma_T = 10\%$. The error tends toward overprediction with increasing mean temperature.

If one assumes that the local temperature fluctuates from shot to shot by 10% of the difference between the local mean temperature and the ambient temperature, this corresponds to a value of σ_T of around 4% at the jet centerline. The systematic error is less than 1% for the speed of sound and less than 5% for the acoustic damping rate. The true temperature fluctuations are likely to be less than the assumed value. Analogous to Fig. 13, the systematic error is plotted as dashed line. It is the difference between the acoustic damping rate at the average temperature and the average acoustic damping rate. Even more so than before, this error contribution is negligible.

Also shown in Figs. 13 and 14 is the result of shot-by-shot intensity fluctuations combined with a threshold below which signals are rejected. See Sec. VII.A for more details.

VI. Challenges

Measurements within the jet at locations closer than $x/D \approx 9$ could only be obtained for a reduced stagnation temperature of 1100 K (Ref. 32). Even very close to the nozzle exit, the first signal peak, although very weak, could be clearly detected over the noise. No additional peaks, however, were visible. In this section, factors influencing the signal intensity and lifetime are addressed.

The issues discussed hereafter fall into two categories: elevated temperatures, where convective effects and turbulence lead to a reduced SNR and reduced signal lifetimes, which in turn increase the measurement uncertainty gradually, and beam steering and vibrations, which, on the other hand, are not well behaved. Below a certain threshold, they have virtually no effect. The density gradients, for example, are too weak to deflect the interrogation beam sufficiently for it to hit the detector. Low-amplitude vibrations do not cause creep of the setup and are usually too slow to have an effect over a signal lifetime ($\sim$1 μs). When they exceed this threshold, measurements are rendered impossible. In the case of beam

Table 1 Normalized peak signal intensities for different run conditions and measurement locations[a]

Run condition	Measurement location	Peak intensity
Off		1.19
Hot jet	Outside jet	1.00
Hot jet	Centerline, $x/D = 15.9$	0.1
Flame	Outside flame and jet	0.08
Flame	Centerline, $x/D = 15.9$	<0.007[b]
Hot jet	In front of jet (Fig. 16a)	0.38
Hot jet	Behind jet (Fig. 16c)	0.49
Hot jet	Within jet (Fig. 16b)	<0.015[b]

[a]The signal intensity when measuring outside the jet, but during operation of the facility, is used as reference. The last three entries correspond to the case shown in Fig. 16 and are taken at $x/D = 0.16$.
[b]No speed of sound data could be extracted.

steering, this occurs when stray light saturates the detector or when the dynamic range of the data acquisition system cannot detect the low-level signal over the background. In the case of vibrations, this point is reached when the setup does not remain stable over the duration of (shot-averaged) measurement.

In the current measurements, it was not possible to separate the effects entirely because the velocity, temperature, and density (perturbation) profiles are strongly correlated in the freejet. The relative importance will vary for different flowfields, experimental facilities, etc.

A. Temperature, Density, and Velocity Effects

As far as the signal intensity scales as p^2T^{-3} for electrostrictive gratings,[30] the peak signal intensity should scale as T^{-3} for a freejet (constant pressure). The expected loss in signal intensity at the nozzle exit ($T_{\text{exit}}/T_\infty \sim 3$), neglecting other factors, is a factor of 30. At $x/D = 15.9$, where the data in Fig. 7 were taken, the centerline temperature is $T \approx 480$ K and the predicted loss factor is four. Compare this to the results shown in Table 1. The signal intensity at this location is found to be 10 times weaker than in the quiescent, ambient air.

Crucial for the accuracy provided by the LIG technique and its applicability for velocimetry is the signal lifetime in terms of the inverse Brillouin and Doppler frequencies. The Brillouin frequency increases with the square root of the temperature. Hence, for a given acoustic damping rate, beam sizes, and, thus, signal lifetime, the number of oscillations in a signal should increase approximately as the square root of the temperature. Figure 6 shows LIG signals obtained at different radial positions at $x/D = 15.9$. The signal lifetime decreases somewhat faster than predicted. As a result, the number of oscillations decreases as well. This is because the acoustic damping rate increases with increasing temperature (dashed line in Fig. 9) and because of the influence of turbulence (Sec. VI.B).

B. Turbulence

When only the case of electrostrictive gratings is considered, three characteristic timescales exist. The acoustic period (inverse Brillouin frequency) is τ_B [Eq. (11)]. The decay time constant for the acoustic damping rate is $\tau_\Gamma = \Lambda^2/\Gamma$. The decay time constant due to finite beam sizes is $\tau_\Omega = \Omega/a$. The signal lifetime depends on τ_Γ and τ_Ω. The number of observable oscillations in the signal can be estimated as

$$M \sim \min(\tau_\Gamma, \tau_\Omega)/\tau_B \tag{13}$$

The quality of the speed of sound data depends critically on the number of oscillations in a signal and their modulation depth. Large-amplitude modulations are more useful for the data analysis than a weakly modulated dc signal. The eddy diffusivity, which has to be added to the acoustic damping rate in Eq. (4), increases the acoustic damping rate. Figure 15 shows how the number of oscillations decreases with increasing signal damping rate, that is, for increasingly dissipative flows or fluids. Oscillations are weighted by their modulation depth relative to the signal amplitude

$$M_{\text{weighted}} = \sum_{i=1}^{M} \frac{\max_i - \min_i}{\max_1} \tag{14}$$

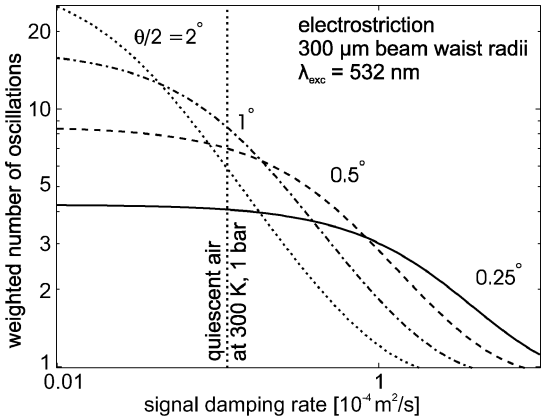

Fig. 15 Number of signal oscillations decreases with increasing acoustic damping rate; larger beam crossing angles are advantageous for quiescent fluids, and smaller beam crossing angles are better in highly dissipative fluids.

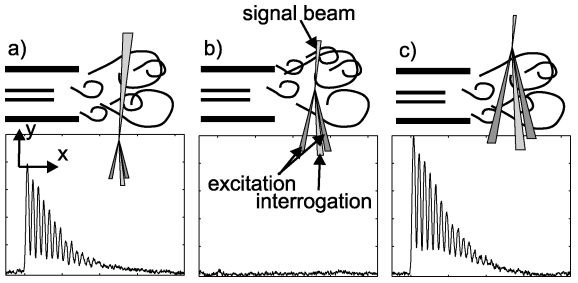

Fig. 16 Signals are detected when measuring at $x/D = 0.16$: a) in front of the jet, c) behind the jet, and b) but not from within the jet; same axes limits are used for all three signals.

M is the number of maxima in the signal, $\max_i$ and $\min_i$ are the signal amplitudes at the ith maximum and minimum, respectively.

The number of interference fringes in the intersection region of the excitation beams is an upper bound for the number of oscillations. This can be observed in Fig. 15 for low acoustic damping rates. M_{weighted} asymptotically approaches this upper bound. The higher the beam crossing angle, the more interference fringes are produced in the intersection region. Hence, for low acoustic damping rates, for example, quiescent gases at high pressures, larger beam crossing angles lead to more oscillations in the signal. The number of oscillations decreases with increasing acoustic damping rate for all beam crossing angles. For highly dissipative fluids, small beam crossing angles are advantageous because the lifetime of the grating is the limiting factor. (See also Sec. VII.B.) Different beam sizes will influence the results quantitatively. Typical beam sizes were assumed in Fig. 15.

C. Beam Steering

To study the influence of beam steering on the signal, measurements were made 5 mm behind the flame holder. The sample volume was shifted in the y direction, that is, signals were acquired when the sample volume was in front of (Fig. 16a), within (Fig. 16b), and behind (Fig. 16c) the jet. Because of the temperature effects addressed in Sec. VI.A, no usable data were obtained from within the jet. If beam steering was responsible for this, then the same result would have been observed at the two other locations. There, however, very good signals were recorded. Their amplitude was approximately one-half of the amplitude observed when measuring below the jet, that is, when none of the beams had to cross the jet (Table 1). In the case of Fig. 16c, a signal can only be observed when all three beams are deflected by the same amount and in the same direction. For the scenario shown in Fig. 16a, only the signal beam has to cross the jet, and its deflection has to be such that it still falls onto the detector. One would, thus, assume that the signal is weaker when measuring

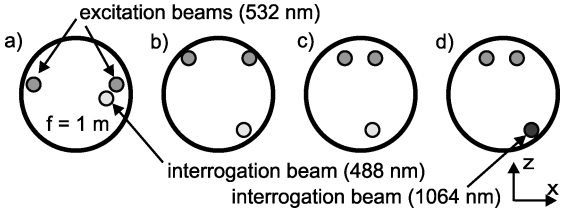

Fig. 17 Pattern of pulsed excitation beams (top) and interrogation beam (bottom) on lens, which focuses all beams onto sample volume (Fig. 3); all beams are parallel.

behind the jet than in front of the jet. This is not observed in the experiment. The difference in peak intensity is not significant. The reason could be that the spacing between the three beams is very small (less than 2 mm) when they enter the jet. They will, therefore, be influenced by the same flow structures.

Brown et al.[33] also examine the influence of beam steering on the signal. It is found that beam steering has no effect on accuracy. They only consider the deflection of the signal beam away from the detector.

Ideally, all beams lie in one plane (as is almost the case in Fig. 17a). This maximizes the overlap between the excitation and interrogation beams, which maximizes the signal intensity, but also the length of the sample volume. It was observed then that one of the excitation beams was deflected sufficiently such that a significant fraction was bleeding through the interference filter, distorting the signal. The setup was changed to the one shown in Fig. 17b. This has only a small effect on the signal level. An advantage of this arrangement is that the length of the sample volume is reduced by approximately 50%. This strategy extended the range of temperatures slightly. To increase Λ and the signal lifetime due to acoustic damping (Fig. 15), a beam arrangement as shown in Fig. 17c was then chosen. The density fluctuations caused a small fraction of the interrogation beam to be deflected onto the detector.

The density gradients in the flow are sufficient to deflect the shoulders of the interrogation beam by an angle of about ψ, that is, the Bragg angle defined by Eq. (5). This provided a dc signal with the actual LIG signal superimposed. The detector noise depends on the total signal. The LIG signal was not detectable within reasonable averaging times within the drastically increased noise level.

D. Vibrations

Vibrations played a significant role in the experiments. After a few iterations, the optical setup was stable enough to produce constant signal levels over several hours. It is, thus, unlikely that changes in the alignment are responsible. This signal level was, however, 20% below the signal level without vibrations (Table 1). This loss can be attributed exclusively to noise-induced vibrations. The cause is likely the reduced laser performance in the presence of vibrations. A drop of the output power of the interrogation laser could be observed on the integrated power monitor. Effects of the vibration on the performance of the excitation laser or on the detector were not examined.

When hydrogen was injected into the center of the jet and combustion was taking place, the noise and vibration level increased significantly. The signal level, measuring outside the jet, dropped to a point where the data could not be analyzed. This is partially due to a further drop of the laser performance and also to vibrations of the optics. After the hydrogen injection ended (after 30–60 s), the signal level returned to only one-half of the precombustion level. Despite repeated efforts, the optics could not be made sufficiently stable to withstand the vibration levels of the supersonic combustion.

The kind and direction of the required adjustments for realignment hint to the causes of the creep: Because of spatial and hardware constraints, the interrogation laser was not securely screwed to the translation table. Its feet rested in cavities of the same diameter. Movements in the vertical direction were not inhibited (during hydrogen injection). Small displacements in the horizontal directions were also possible (creep). The inertia of the laser was not sufficient to prevent these movements above a certain vibration threshold. The optical components were mounted on three optical breadboards, which, in turn, were clamped individually to the translation table. Although impossible to observe directly, vibrations appear to have induced relative motion between the breadboards.

VII. Opportunities

Despite the experiences from the measurements presented, which appear to rule out LIGs for combustion environments at atmospheric pressures or below, improvements by several orders of magnitude are possible with off-the-shelf equipment. The main issues are signal intensity and lifetime. The latter is particularly important for velocimetry applications.

A. Signal Intensity

Hart et al.[31,34] made speed of sound measurements in quiescent air at atmospheric pressure for temperatures up to 650 K. The highest measured temperature in the data presented earlier is 540 K at $x/D = 9.6$ (Fig. 7). If one assumes that a T^{-3} dependence is observed for fluids at rest and that the $T^{-4.25}$ behavior (Fig. 11) is due to flow effects, note that

$$(650/273)^{-3} \approx (540/273)^{-4.25} \tag{15}$$

The two measurement conditions are comparable with respect to signal intensity when discounting for the airflow. Hart et al.[34] used a 70-mJ excitation pulse and a pulsed interrogation beam with a pulse power of 3 kW. They were able to obtain highly accurate single-shot data.

Temperatures in supersonic combustion facilities exceed 2000 K. If a T^{-3}–T^{-4} scaling is assumed (Sec. VI.A), this corresponds to signal levels that are two orders of magnitude below those observed for the hottest measurements presented in Sec. IV. Compared to room temperature, the signal amplitude drops by three orders of magnitude. If an even stronger T^{-6} dependence for thermal gratings is assumed,[30] laser-induced thermal gratings for high-temperature applications at and below atmospheric pressures are probably not realistic.

The peak signal amplitude for a given temperature and pressure scales with the square of the pulse energy of the excitation laser and linearly with the interrogation laser power.[35] Gas breakdown is observed for pulse energies above a certain threshold. For ambient conditions and high beam qualities, gas breakdowns can be observed at pulse energies of 50 mJ (Ref. 3) for spot sizes of approximately 100 μm. In practice, pulse energies cannot be raised well above 100 mJ for spot sizes of a few hundred micrometers. Jenkins et al.[36] use 800-mJ pulses at 1064 nm, but with spot sizes of 2.5 mm. The theoretical models assume acoustic, that is, weak, waves, an assumption that fails for high pulse energies and that results in measurement errors.

Despite its weaker influence, the largest potential is, thus, the use of pulsed interrogation lasers. LIG signals last a few hundred nanoseconds to 1 μs. Consider a long-pulse YAG with 100-mJ, 1-μs pulses. This corresponds to a laser power of 10^5 W for the duration of the pulse, which is four orders of magnitude above powers achievable with a continuous-wave laser (excluding CO_2 lasers). Excitation and interrogation lasers at the same wavelength would result in strong cross talk because stray light from the excitation laser could not be filtered out and would fall onto the detector. Hart et al.[31,34] and Stevens and Ewart[5] use a long-pulsed alexandrite laser at 750 nm as an interrogation light source. If a dual-cavity Nd:YAG is to be used for both purposes, one has to be frequency doubled. (Other combinations of the fundamental wavelength and harmonics or combinations of different harmonics are also possible.) The generation of harmonics is more efficient for Q-switched operation. The frequency-doubled beam should, thus, be used for excitation and the infrared beam for interrogation. This is also advantageous from the point of view of beam steering (Sec. VII.B). The quantum efficiency of photomultiplier tubes working in the infrared is one order of magnitude below of those working in the visible spectral range, for example, 10% quantum efficiency for a Hamamatsu

H6780 at 488 nm vs 1% quantum efficiency for a Hamamatsu H9170 at 1064 nm. The signal amplitudes will, thus, not increase by as much as the interrogation beam power.

Beam steering results in a large shot-by-shot variation of the signal strength. The averaged signals are predominantly made up of a few strong signals, whereas the remaining shots only contribute to noise. The SNR can be improved by only utilizing data from those shots with good signal levels, as proposed in Ref. 33. The result of such an approach is shown in Figs. 13 and 14 for one (arbitrary) condition. When the same procedure as described in Sec. V.D was followed, it was assumed that beam steering effects cause shot-by-shot intensity fluctuations with $\sigma_L = 25\%$ standard deviation in Eq. (9). Signals with a peak amplitude below unity were rejected from the averaging before data analysis. This increases the tendency to underpredict sound speeds and temperatures. The chosen values for σ_L and the threshold are arbitrary, but other parameters will show the same qualitative outcome.

B. Signal Lifetime

For highly turbulent flows, $\tau_\Gamma \ll \tau_\Omega$ (Sec. VI.B), that is, signal damping (including eddy diffusivity) is the mechanism limiting the signal lifetime. Then τ_Γ scales as Λ^2, whereas τ_B, on the other hand, only scales linearly with Λ. The signal lifetime with respect to the acoustic period [M, Eq. (13)], thus, scales linearly with Λ. It can be increased by increasing the excitation laser wavelength or by reducing the excitation beam crossing angle.

On the one hand, θ should be as small as possible to maximize the fringe spacing Λ and, thus, the signal lifetime. On the other hand, ψ should be as large as possible to maximize the angular spacing of the interrogation and the signal beam. The Bragg condition [Eq. (5)] relates θ linearly to ψ for given laser wavelengths. Both can only be achieved by variations of $\lambda_{\text{exc}}/\lambda_{\text{int}}$. Beam steering (too small ψ) was the limiting factor in the measurements performed here. For a given λ_{exc}, the size of the mirror mounts limits Λ. With the optical components used, $\theta/2 \leq 0.25$ deg could be achieved, but beam steering rendered these setups useless (Sec. VI.C).

Using a frequency-doubled Nd:YAG as an excitation laser and a Nd:YAG at the fundamental frequency would result in a beam arrangement as shown in Fig. 17d. The angular separation between signal and interrogation beams could be maintained for smaller excitation beam crossing angles. By this simple change, signal lifetimes could be increased by a factor of three to four, or more with additional changes in the setup of the optical mounts. Because of the angle at which the interrogation laser intercepts the plane formed by the excitation beams (Figs. 17d and 4b), the length of the sample volume would not increase.

C. Hardware

Noise-induced vibrations influenced the measurements twofold: They degraded the performance of the light sources (and potentially of the detector), and they caused creeping misalignments of the optics. The flashlamp-pumped Nd:YAG laser dated from the 1980s. A gas laser was used as interrogation light source. It is expected that modern, fully solid-state lasers will perform significantly better in this environment. The sensitivity toward vibrations will be model specific. Because of the high peak powers, fiber delivery for the Q-switched excitation laser radiation is not feasible. The key to using a long-pulse Nd:YAG interrogation laser is its temporal profile. In previous tests, mode beatings in the same range as the Brillouin frequency were observed. The misalignments introduced by the vibrations (Sec. VI.D) are not intrinsic to LIGs and can be solved, potentially, by placing the optics and lasers in a vibration isolating housing.

An alternative approach uses two Q-switched lasers at different harmonics. The delay of the interrogation pulse relative to the excitation pulse sweeps from zero to the signal lifetime. The step size is chosen to be less than the pulse duration. A complete LIG signal is assembled from such a series. Single-shot operation and velocimetry are not possible with this approach, but interrogation beam powers are on the order of 10 MW (100 mJ and 10 ns). The signal intensity is proportional to the interrogation beam power. Averaging over n signals with a 1-μs interrogation pulse yields, thus, the same result as assembling a series from n Q-switched interrogation pulses as described earlier. The long-pulse operation provides more flexibility and allows velocimetry. Q-switched lasers, however, have a well-defined temporal beam profile and are more easily available.

VIII. Conclusions

Turbulence, convective effects, and beam steering each significantly reduce the SNR of transient LIG thermometry. This is in addition to the T^{-3} signal loss for electrostrictive gratings. The gas breakdown threshold provides an upper bound for the excitation pulse energy. It is concluded that the upper bound for temperatures, where transient LIG thermometry is applicable, cannot be extended significantly above ~650 K for quiescent fluids and ~550 K for highly turbulent compressible flows (assuming atmospheric pressure) using a continuous-wave interrogation laser.

It is concluded that by employing a multikilowatt pulsed interrogation laser and excitation pulse intensities close to the gas breakdown threshold, shot-averaged thermometry is possible for temperatures observed in supersonic combustion test facilities. This assumes that signal lifetimes of several acoustic periods can still be achieved at smaller beam crossing angles. (For highly dissipative flows, the signal lifetime increases faster than the acoustic period with decreasing beam crossing angle/increasing fringe spacing.) The signal lifetime required for velocimetry can be estimated as the required lifetime for thermometry divided by the Mach number. In high-speed subsonic, transonic, and supersonic flows, it is expected that when thermometry is possible, so will be velocimetry.

In a hot, turbulent, supersonic, compressible jet, beam steering effects were found to be the limiting factor for the technique. When laser wavelengths are selected, longer, wavelengths have to be favored for the interrogation beam. In quiescent fluids, finite signal lifetime effects dominate. Here, the longer wavelength is preferably used for the excitation laser, which results in a larger grating fringe spacing for a given beam crossing angle.

Acknowledgments

This work was partially supported by the Collaborative Research Center (Sonderforschungsbereich) 259 (High-Temperature Problems of Reusable Space Transportation Systems).

References

[1]Butenhoff, T. J., "Measurement of the Thermal-Diffusivity and Speed of Sound of Hydrothermal Solutions via the Laser-Induced Grating Technique," *International Journal of Thermophysics*, Vol. 16, No. 1, 1995, pp. 1–9.

[2]Cummings, E. B., Hornung, H. G., Brown, M. S., and DeBarber, P. A., "Measurement of Gas-Phase Sound Speed and Thermal Diffusivity over a Broad Pressure Range Using Laser-Induced Thermal Acoustics," *Optics Letters*, Vol. 20, No. 14, 1995, pp. 1577–1579.

[3]Schlamp, S., Hornung, H. G., Sobota, T. H., and Cummings, E. B., "Accuracy and Uncertainty of Single-Shot, Nonresonant Laser-Induced Thermal Acoustics," *Applied Optics*, Vol. 39, No. 30, 2000, pp. 5477–5481.

[4]Stampanoni-Panariello, A., Hemmerling, B., and Hubschmid, W., "Temperature Measurements in Gases Using Laser-Induced Electrostrictive Gratings," *Applied Physics B—Lasers and Optics*, Vol. 67, No. 1, 1998, pp. 125–130.

[5]Stevens, R., and Ewart, P., "Single-Shot Measurement of Temperature and Pressure Using Laser-Induced Thermal Gratings with a Long Probe Pulse," *Applied Physics B—Lasers and Optics*, Vol. 78, No. 1, 2004, pp. 111–117.

[6]Li, Y. Y., Roberts, W. L., and Brown, M. S., "Investigation of Gaseous Acoustic Damping Rates by Transient Grating Spectroscopy," *AIAA Journal*, Vol. 40, No. 6, 2002, pp. 1071–1077.

[7]Brown, M. S., and Roberts, W. L., "Single-Point Thermometry in High-Pressure, Sooting, Premixed Combustion Environments," *Journal of Propulsion and Power*, Vol. 15, No. 1, 1999, pp. 119–127.

[8]Latzel, H., Dreizler, A., Dreier, T., Heinze, J., Dillmann, M., Stricker, W., Lloyd, G. M., and Ewart, P., "Thermal Grating and Broadband Degenerate Four-Wave Mixing Spectroscopy of OH in High-Pressure Flames," *Applied Physics B—Lasers and Optics*, Vol. 67, No. 5, 1998, pp. 667–673.

[9]Hart, R. C., Balla, R. J., and Herring, G. C., "Simultaneous Velocimetry and Thermometry of Air by Use of Nonresonant Heterodyned Laser-Induced Thermal Acoustics," *Applied Optics*, Vol. 40, No. 6, 2001, pp. 965–968.

[10]Barker, P. F., Thomas, A. M., McIntyre, T. J., and Rubinsztein-Dunlop, H., "Velocimetry and Thermometry of Supersonic Flow Around a Cylindrical Body," *AIAA Journal*, Vol. 36, No. 6, 1998, pp. 1055–1060.

[11]Barker, P. F., Grinstead, J. H., and Miles, R. B., "Single-Pulse Temperature Measurement in Supersonic Air Flow with Predissociated Laser-Induced Thermal Gratings," *Optics Communications*, Vol. 168, No. 1–4, 1999, pp. 177–182.

[12]Walker, D. J. W., Williams, R. B., and Ewart, P., "Thermal Grating Velocimetry," *Optics Letters*, Vol. 23, No. 16, 1998, pp. 1316–1318.

[13]Hemmerling, B., Kozlov, D. N., and Stampanoni-Panariello, A., "Temperature and Flow-Velocity Measurements by Use of Laser-Induced Electrostrictive Gratings," *Optics Letters*, Vol. 25, No. 18, 2000, pp. 1340–1342.

[14]Hemmerling, B., Neracher, M., Kozlov, D., Kwan, W., Stark, R., Klimenko, D., Clauss, W., and Oschwald, M., "Rocket Nozzle Cold-Gas Flow Velocity Measurements Using Laser-Induced Gratings," *Journal of Raman Spectroscopy*, Vol. 33, No. 11–12, 2002, pp. 912–918.

[15]Schlamp, S., "Laser-Induced Thermal Acoustic Velocimetry," Ph.D. Dissertation, Graduate Aeronautical Lab., California Inst. of Technology, Pasadena, CA, June 2000.

[16]Schlamp, S., Cummings, E. B., and Sobota, T. H., "LITA Velocimetry Using Heterodyne Detection," *Optics Letters*, Vol. 25, No. 4, 2000, pp. 224–226.

[17]Schlamp, S., and Allen-Bradley, E., "Homodyne Detection Laser-Induced Thermal Acoustics Velocimetry," AIAA Paper 2000-0376, Jan. 2000.

[18]O'Byrne, S., Danehy, P. M., and Cutler, A. D., "Dual-Pump CARS Thermometry and Species Concentration Measurements in a Supersonic Combustor," AIAA Paper 2004-0710, Jan. 2004.

[19]McIntyre, T. J., Houwing, A. F. P., Palma, P. C., and Rabbath, P., and Fox, J. S., "Imaging of Combustion in a Supersonic-Combustion Ramjet," *Journal of Propulsion and Power*, Vol. 13, No. 3, 1996, pp. 388–394.

[20]Forkey, J. N., Lempert, W. R., and Miles, R. B., "Accuracy Limits for Planar Measurements of Flow Field Velocity, Temperature and Pressure Using Filtered Rayleigh Scattering," *Experiments in Fluids*, Vol. 24, No. 2, 1998, pp. 151–162.

[21]Trusler, J. P. M., *Physical Acoustics and Metrology of Fluids*, Adam Hilger, Bristol, England, U.K., 1991, pp. 15, 16.

[22]Kasal, P., and Algermissen, J., "Temperature Measurements by Raman-Spectroscopy in Hydrogen Air Supersonic Flames Induced by Oblique Shocks," *Zeitschrift für Flugwissenschaften und Weltraumforschung*, Vol. 13, No. 6, 1989, pp. 399–404.

[23]Kasal, P., Gerlinger, P., Walther, R., von Wolfersdorf, J., and Weigand, B., "Supersonic Combustion: Fundamental Investigations of Aerothermodynamic Key Problems," AIAA Paper 2002-5119, Sept. 2002.

[24]Anderson, S. M., and Bremhorst, K., "Investigation of the Flow Field of a Highly Heated Jet of Air," *International Journal of Heat and Fluid Flow*, Vol. 23, No. 2, 2002, pp. 205–219.

[25]Hart, R. C., Balla, R., Herring, G. C., and Jenkins, L., "Seedless Laser Velocimetry Using Heterodyne Laser Induced Thermal Acoustics," Technical Rept. 2001-19, ICASE, Aug. 2001.

[26]Cummings, E. B., Leyva, I. A., and Hornung, H. G., "Laser-Induced Thermal Acoustics (LITA) Signals from Finite Beams," *Applied Optics*, Vol. 34, No. 18, 1995, pp. 3290–3302.

[27]Cummings, E. B., "Laser-Induced Thermal Acoustics," Ph.D. Dissertation, Graduate Aeronautical Lab., California Inst. of Technology, Pasadena, CA, June 1995.

[28]Hyland, R. W., and Wexler, A., "Formulations for the Thermodynamic Properties of Dry Air from 173.15 K to 473.15 K, and for Saturated Moist Air from 173.15 K to 473.15 K, at Pressures to 5 MPa," *Transactions of the Americal Society for Heating, Refrigerating and Air-conditioning Engineers*, Vol. 89, No. 5, 1983, pp. 520–535.

[29]Hansen, C. F., "Approximation for the Thermodynamic and Transport Properties of High-Temperature Air," NASA TR-R-50, Jan. 1959.

[30]Danehy, P. M., "Population- and Thermal-Grating Contributions to Degenerate Four-Wave Mixing," Ph.D. Dissertation, Dept. of Mechanical Engineering, Stanford Univ., Stanford, CA, June 1995.

[31]Hart, R. C., Balla, R. J., and Herring, G. C., "Optical Measurement of the Speed of Sound in Air over the Temperature Range 300–650 K," *Journal of the Acoustical Society of America*, Vol. 108, No. 4, 2000, pp. 1946–1948.

[32]Schlamp, S., Kasal, P., Rösgen, T., and Weigand, B., "Experimental Considerations for Laser-Induced Thermoacoustics in Compressible Turbulent Flows," AIAA Paper 2003-3454, June 2003.

[33]Brown, M. S., Li, Y. Y., Roberts, W. L., and Gord, J. R., "Analysis of Transient-Grating Signals for Reacting-Flow Applications," *Applied Optics*, Vol. 42, No. 3, 2003, pp. 566–578.

[34]Hart, R. C., Balla, R. J., and Herring, G. C., "Nonresonant Referenced Laser-Induced Thermal Acoustics Thermometry in Air," *Applied Optics*, Vol. 38, No. 3, 1999, pp. 577–584.

[35]Panariello, A. C. S., "Laser-Induced Gratings in the Gas Phase: Formation Mechanisms and Applications for Diagnostics," Ph.D. Dissertation, Physics Dept., Swiss Federal Inst. of Technology, Zurich, 2003.

[36]Jenkins, L. N., Hart, R. C., Balla, R. J., Herring, G. C., Khorrami, M. R., and Choudhari, M. M., "Application of Laser-Induced Thermal Acoustics to a High-Lift Configuration," *Optical Diagnostics for Fluids, Solids, and Combustion II*, edited by P. V. Farrell, F.-P. Chiang, C. R. Mercer, and G. Shen, Vol. 5191, Proceedings of the SPIE, Aug. 2003, pp. 134–144.